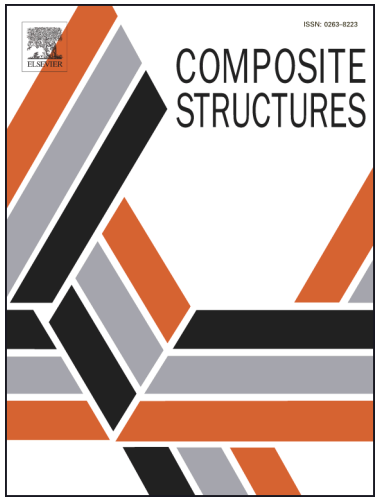

Free and forced vibrations of functionally graded polymer composite plates reinforced with graphene nanoplatelets

Mitao Song, Sritawat Kitipornchai, Jie Yang

PII: S0263-8223(16)31467-2
DOI: http://dx.doi.org/10.1016/j.compstruct.2016.09.070
Reference: COST 7796

To appear in: *Composite Structures*

Received Date: 8 August 2016
Revised Date: 23 September 2016
Accepted Date: 24 September 2016

Please cite this article as: Song, M., Kitipornchai, S., Yang, J., Free and forced vibrations of functionally graded polymer composite plates reinforced with graphene nanoplatelets, *Composite Structures* (2016), doi: http://dx.doi.org/10.1016/j.compstruct.2016.09.070

Free and forced vibrations of functionally graded polymer composite plates reinforced with graphene nanoplatelets

Mitao Song [a, b], Sritawat Kitipornchai [a], Jie Yang [c,*]

[a] *School of Civil Engineering, The University of Queensland, St Lucia, Brisbane, QLD 4072 Australia*

[b] *Faculty of Civil Engineering and Mechanics, Jiangsu University, Zhenjiang, Jiangsu, 212013 P.R. China*

[c] *School of Engineering, RMIT University, PO Box 71, Bundoora, VIC 3083 Australia*

Free and forced vibrations of functionally graded polymer composite plates reinforced with graphene nanoplatelets

Mitao Song [a, b], Sritawat Kitipornchai [a], Jie Yang [c,*]

[a] *School of Civil Engineering, The University of Queensland, St Lucia, Brisbane, QLD 4072 Australia*

[b] *Faculty of Civil Engineering and Mechanics, Jiangsu University, Zhenjiang, Jiangsu, 212013 P.R. China*

[c] *School of Engineering, RMIT University, PO Box 71, Bundoora, VIC 3083 Australia*

Abstract

This paper investigates the free and forced vibration characteristics of functionally graded multilayer graphene nanoplatelet (GPL)/polymer composite plates within the framework of the first-order shear deformation plate theory. The weight fraction of GPL nanofillers shows a layer-wise variation along the thickness direction with GPLs uniformly dispersed in the polymer matrix in each individual layer. The effective Young's modulus is predicted by the modified Halpin-Tsai model while the effective Poisson's ratio and mass density are determined by the rule of mixture. Governing differential equations of motion are derived and Navier solution based technique is employed to obtain the natural frequencies and dynamic response of simply supported functionally graded GPL/polymer plates under a dynamic loading. A parametric study is conducted, with a particular focus on the effects of GPL distribution pattern, weight fraction, geometry and size as well as the total number of layers on the dynamic characteristics of the plates.

Keywords: Graphene nanoplatelets; Functionally grade materials; Polymer composites; Multilayer plate; The first-order shear deformation plate theory; Dynamic behavior.

---

[*] Corresponding author. Tel.: 61-03-99256169; Fax: 61-03-99256108

E-mail address: j.yang@rmit.edu.au (J. Yang)

1. Introduction

Owing to their extraordinary mechanical, thermal and electrical properties, carbon-filled polymer composites have been widely used in various engineering sectors including aerospace, automotive, biomedical, and civil engineering in the past two decades [1-4]. Compared with other carbon-based nanofillers, graphene or graphene platelets (GPLs) have extremely high specific surface areas with lower production cost, making them excellent candidates as the reinforcement materials in composites [5]. It has been theoretically and experimentally observed that the addition of even a very small amount of graphene into the pristine polymer matrix can dramatically improve its mechanical [6-10], thermal [11, 12], and electrical properties [12]. This creates a great opportunity for the development of advanced light weight structures made of graphene based polymer nanocomposites.

So far, the majority of the research efforts in this emerging area have been devoted to the synthesis, fabrication, and material property characterization of graphene based composites with low content of graphene fillers. Rafiee et al. [6] demonstrated that by adding 0.1% weight fraction (w.t.%) of GPLs, the strength and stiffness of the reinforced polymer composites are enhanced by the same degree achieved by adding 1.0 w.t.% of carbon nanotubes (CNTs). By embedding 6.0 w.t.% of GPLs in the epoxy matrix, King et al. [13] manufactured GPL/epoxy nanocomposites whose Young's modulus increases from 2.72 GPa to 3.36 GPa. Fang et al. [14] fabricated polystyrene sheet nanocomposites with the incorporation of 0.9 w.t.% of graphene sheets, leading to a significant increase of 57.2% in Young's modulus. Zhao et al. [15] manufactured graphene based polyvinyl alcohol by adding 1.8% volume fraction of graphene oxide into polyvinyl alcohol matrix and obtained a nanocomposite with Young's modulus 10 times greater than that of the pristine sample. Wang et al. [16] studied the effects of different GPL sizes on the mechanical properties of GPL/epoxy nanocomposites and their study indicated that a larger GPL size can significantly improve the tensile modulus but reduce the strength of the nanocomposites.

Besides the experimental efforts, some theoretical and numerical investigations on the mechanical performance of graphene based composites have also been carried out. Based on Mori-Tanaka model, Ji et al. [17] developed a micromechanics methods to study the effective elastic properties of

graphene/polymer composites. Rahman and Haque [18] investigated the effects of GPL concentrations, aspect ratios and dispersion on elastic constants and stress-strain responses of GPL/epoxy composites using molecular mechanics and molecular dynamics simulations. Liu et al. [19] carried out the study on the effects of wrinkles of graphene sheet, polymer matrix type, polymer molecule chain length and pull-out velocity on the interfacial mechanical properties of graphene enhanced nanocomposites by employing the molecular dynamics simulations. Montazeri and Rafii-Tabar [10] employed a molecular structural mechanics/finite element-based multiscale modeling approach to examine the effects of GPLs on Young's modulus of the polymer matrix. Spanos et al. [20] estimated the elastic mechanical properties of graphene reinforced composites by using a multiscale finite element method in which the atomistic molecular structural mechanics approach was combined with the continuum finite element method.

Understanding the dynamic behavior of carbon-based composites and structures is crucial for their engineering applications. The static bending, elastic buckling, postbuckling, linear and nonlinear free and forced vibrations of CNT reinforced composite structures have been extensively investigated [21-28]. Among those dealing with the dynamic behavior of graphene reinforced composites and structures, Long et al. [29] employed molecular dynamic simulation for the shock response of graphene/Cu nanolayered composite and discussed the deformation and spall damage of Cu, delamination of the nanolaminates, wrinkling and fracture of graphene. Rissanou et al. [30] studied the effect of the size of graphene sheets on structural and dynamical properties of several graphene based polymer nanocomposite systems by using detailed atomistic molecular dynamics simulations. Chandra et al. [31] presented a multiscale approach for the natural frequencies of graphene/polymer composite structures by modeling graphene at the atomistic scale and the matrix deformation by the continuum finite element method. It should be noted that researches on the dynamic behavior of graphene based nanocomposite structures are still very limited. To the best of authors' knowledge, all of the previous studies on material fabrication and mechanical behavior analysis considered nanocomposites reinforced with graphene nanofillers uniformly dispersed in the matrix only. No work has been done on nanocomposites and structures with non-uniformly distributed graphene reinforcements.

Functionally graded materials (FGMs) are characterized by continuous variations in both material composition and mechanical properties in one or more dimension(s) which can be tailored to simultaneously meet different performance requirements. Due to the constraint of current manufacturing technology, the fabrication of an ideal FGM structure with GPL concentration varying continuously over thickness direction is extremely difficult if not impossible. A multilayer structure consisting of a number of individual layers stacked up in which GPL weight fraction remains constant within each layer but follows a layer-wise gradual change through thickness is an excellent alternative if the total number of layers is sufficiently large. The present paper aims to investigate the dynamic performance of such functionally graded GPL/polymer nanocomposite plates under a transverse dynamic load. The modified Halpin-Tsai model is employed to predict the effective Young's modulus while the rule of mixture is used to determine the effective Poisson's ratio and mass density. Theoretical formulations are based on the first-order shear deformation plate theory. Double Fourier series solution in combination of Navier solution based technique is utilized to obtain the natural frequencies and the dynamic deflection response of the simply supported plate. A detailed numerical study are conducted to shed important insights into the effects of the distribution pattern, weight fraction, geometry and size of GPLs as well as the total number of layers on the free and forced vibrations of the functionally graded GPL/polymer nanocomposite plate.

2. Problem Formulation

A multi-layer GPL/polymer nanocomposite plate with length a, width b and thickness h subjected to a distributed transverse dynamic load $F(X, Y, T)$ is shown in Fig. 1. The plate is composed of N_L layers with the same thickness $\Delta h = h / N$ and is reinforced by GPLs uniformly dispersed in the polymer matrix in each individual layer. The GPL weight fraction (w.t.%) shows a layer-wise variation to form a functionally graded structure. In order to investigate the effect of GPL distribution on the dynamic performance of the GPL/polymer plate, four different GPL distribution patterns shown in Fig. 2 are considered, among which Pattern 1 is a special case corresponding to an isotropic homogeneous plate in which GPLs are uniformly distributed at the same w.t.% across all layers. Patterns 2-4 represent,

respectively, a graded material composition where GPL weight fraction changes linearly from layer to layer along the plate thickness. The GPL weight fraction decreases from the highest in the midplane to the lowest on both top and bottom surfaces of the plate in Pattern 2 while in Pattern 3, this is reversed with the maximum weight fraction on both top and bottom surfaces and the lowest in the midplane of the plate. It should be noted that both Pattern 2 and Pattern 3 are symmetric whereas in non-symmetrical Pattern 4, GPL weight fraction increases linearly from the top surface to the bottom surface.

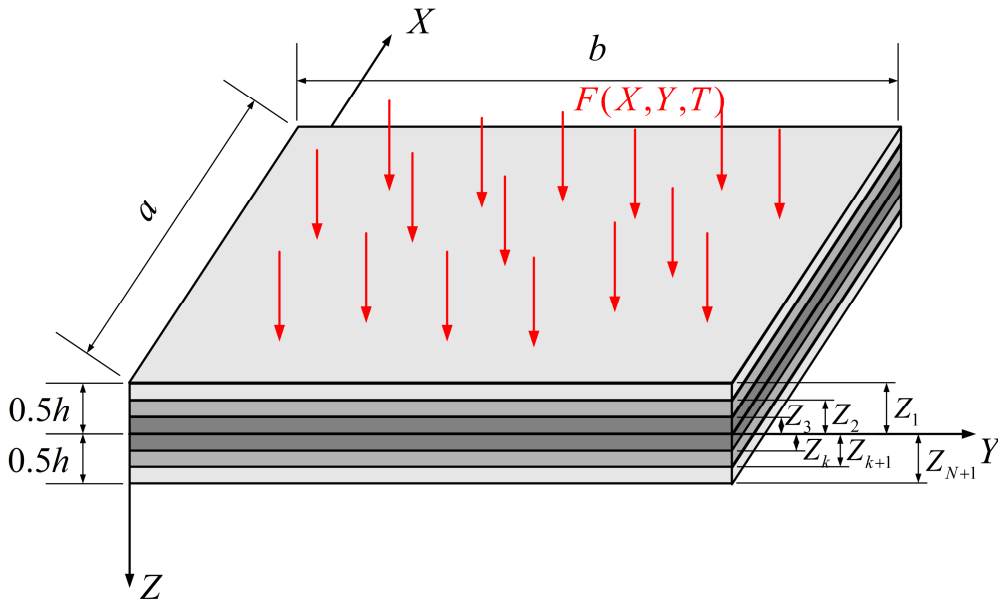

Fig. 1. A multi-layer functionally graded GPL/polymer nanocomposite plate

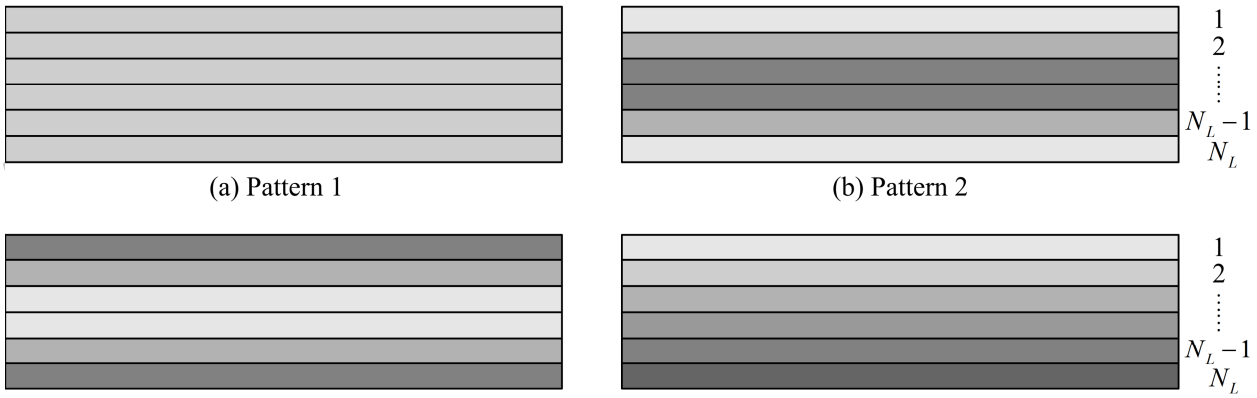

Fig. 2. Different GPL distribution patterns

2.1 Effective Material Properties

Modified Halpin-Tsai model is used to calculate the effective Young's modulus of the GPL/polymer composite. Assuming GPLs as effective rectangular solid fillers uniformly dispersed in a polymer matrix, effective Young's modulus of the GPL/polymer composite, E_C, can be approximated by Voigt-Reuss model [32]:

$$E_C = \frac{3}{8}E_{\square} + \frac{5}{8}E_{\perp} \tag{1}$$

where longitudinal modulus $E_{\square}$ and transverse modulus $E_{\perp}$ can be determined by Halpin-Tsai model [33]:

$$E_{\square} = \frac{1+\xi_L \eta_L V_{GPL}}{1-\eta_L V_{GPL}} \times E_M \tag{2}$$

$$E_{\perp} = \frac{1+\xi_W \eta_W V_{GPL}}{1-\eta_W V_{GPL}} \times E_M \tag{3}$$

Substituting Eqs (2) and (3) into Eq. (1) yields

$$E_C = \frac{3}{8}\frac{1+\xi_L \eta_L V_{GPL}}{1-\eta_L V_{GPL}} \times E_M + \frac{5}{8}\frac{1+\xi_W \eta_W V_{GPL}}{1-\eta_W V_{GPL}} \times E_M \tag{4}$$

where

$$\eta_L = \frac{(E_{GPL}/E_M)-1}{(E_{GPL}/E_M)+\xi_L} \tag{5}$$

$$\eta_W = \frac{(E_{GPL}/E_M)-1}{(E_{GPL}/E_M)+\xi_W} \tag{6}$$

E_M and E_{GPL} are Young's moduli of the polymer matrix and GPLs, respectively, V_{GPL} is GPL volume fraction, ξ_L and ξ_W are the parameters characterizing both the geometry and size of GPL nanofillers, defined as

$$\xi_L = 2\left(\frac{l_{GPL}}{h_{GPL}}\right) \tag{7}$$

$$\xi_{\mathrm{W}} = 2\left(\frac{w_{\mathrm{GPL}}}{h_{\mathrm{GPL}}}\right) \tag{8}$$

in which l_{GPL}, w_{GPL} and h_{GPL} are the average length, width, and thickness of the GPLs, respectively. Mass density ρ_{C} and Possion's ratio ν_{C} of the GPL/ polymer nanocomposite can be calculated by rule of mixture

$$\rho_{\mathrm{C}} = \rho_{\mathrm{GPL}} V_{\mathrm{GPL}} + \rho_{\mathrm{M}} V_{\mathrm{M}} \tag{9}$$

$$\nu_{\mathrm{C}} = \nu_{\mathrm{GPL}} V_{\mathrm{GPL}} + \nu_{\mathrm{M}} V_{\mathrm{M}} \tag{10}$$

where V_{M} is the volume fraction of polymer matrix, subscripts "GPL", "M" and "c" stand for GPLs, polymer matrix and GPL/polymer nanocomposite, respectively. The volume fraction of GPLs, denoted by V_{GPL}, is given by

$$V_{\mathrm{GPL}} = \frac{g_{\mathrm{GPL}}}{g_{\mathrm{GPL}} + (\rho_{\mathrm{GPL}}/\rho_{\mathrm{M}})(1 - g_{\mathrm{GPL}})} \tag{11}$$

where g_{GPL} is weight fraction of GPLs in the nanocomposite.

2.2 Governing Equation

According to the first-order shear deformation plate theory [34], the displacements of an arbitrary point in the plate are

$$\begin{aligned} U(X,Y,Z,T) &= u_0(X,Y,T) + Z\phi_x(X,Y,T) \\ V(X,Y,Z,T) &= v_0(X,Y,T) + Z\phi_y(X,Y,T) \\ W(X,Y,Z,T) &= w_0(X,Y,T) \end{aligned} \tag{12}$$

where $u_0(X,Y,T)$, $v_0(X,Y,T)$ and $w_0(X,Y,T)$ are the mid-plane displacement components of the plate, and T is time. Note that

$$\phi_x = \frac{\partial U}{\partial Z}, \quad \phi_y = \frac{\partial V}{\partial Z} \tag{13}$$

which represent the rotations of the cross-section about the Y and X axes, respectively. The linear strain-displacement relationship gives

$$\begin{Bmatrix} \varepsilon_{xx} \\ \varepsilon_{yy} \\ \gamma_{xy} \\ \gamma_{yz} \\ \gamma_{xz} \end{Bmatrix} = \begin{Bmatrix} \varepsilon_{xx}^{(0)} \\ \varepsilon_{yy}^{(0)} \\ \gamma_{xy}^{(0)} \\ \gamma_{yz}^{(0)} \\ \gamma_{xz}^{(0)} \end{Bmatrix} + Z \begin{Bmatrix} \varepsilon_{xx}^{(1)} \\ \varepsilon_{yy}^{(1)} \\ \gamma_{xy}^{(1)} \\ \gamma_{yz}^{(1)} \\ \gamma_{xz}^{(1)} \end{Bmatrix} \tag{14}$$

where

$$\begin{Bmatrix} \varepsilon_{xx}^{(0)} \\ \varepsilon_{yy}^{(0)} \\ \gamma_{xy}^{(0)} \\ \gamma_{yz}^{(0)} \\ \gamma_{xz}^{(0)} \end{Bmatrix} = \begin{Bmatrix} \dfrac{\partial u_0}{\partial X} \\ \dfrac{\partial v_0}{\partial Y} \\ \dfrac{\partial u_0}{\partial Y} + \dfrac{\partial v_0}{\partial X} \\ \dfrac{\partial w_0}{\partial Y} + \phi_y \\ \dfrac{\partial w_0}{\partial X} + \phi_x \end{Bmatrix} \tag{15}$$

and

$$\begin{Bmatrix} \varepsilon_{xx}^{(1)} \\ \varepsilon_{yy}^{(1)} \\ \gamma_{xy}^{(1)} \\ \gamma_{yz}^{(1)} \\ \gamma_{xz}^{(1)} \end{Bmatrix} = \begin{Bmatrix} \dfrac{\partial \phi_x}{\partial X} \\ \dfrac{\partial \phi_y}{\partial Y} \\ \dfrac{\partial \phi_x}{\partial Y} + \dfrac{\partial \phi_y}{\partial X} \\ 0 \\ 0 \end{Bmatrix} \tag{16}$$

The stress components of the *k*th layer can be obtained from the linear elastic stress-strain constitutive relationship as

$$\begin{Bmatrix} \sigma_{xx} \\ \sigma_{yy} \\ \sigma_{xy} \\ \sigma_{yz} \\ \sigma_{xz} \end{Bmatrix}^{(k)} = \begin{bmatrix} [P] & [0] \\ [0] & [Q] \end{bmatrix}^{(k)} \begin{Bmatrix} \varepsilon_{xx} \\ \varepsilon_{yy} \\ \gamma_{xy} \\ \gamma_{yz} \\ \gamma_{xz} \end{Bmatrix}^{(k)} \tag{17}$$

where

$$P_{11}^{(k)} = P_{22}^{(k)} = \frac{E_C^{(k)}}{1-\nu_C^2}, \quad P_{12}^{(k)} = P_{21}^{(k)} = \frac{\nu E_C^{(k)}}{1-\nu_C^2},$$
$$P_{33}^{(k)} = Q_{11}^{(k)} = Q_{22}^{(k)} = \frac{E_C^{(k)}}{2(1+\nu_C)}, \quad P_{13}^{(k)} = P_{31}^{(k)} = P_{23}^{(k)} = P_{32}^{(k)} = Q_{12}^{(k)} = Q_{21}^{(k)} = 0 \tag{18}$$

Based on Hamilton's principle, the governing equations of motion of the GPL/polymer nanocomposite plate subjected to a dynamic load $F(X, Y, T)$ can be derived as

$$\frac{\partial N_{xx}}{\partial X} + \frac{\partial N_{xy}}{\partial Y} = \bar{I}_0 \frac{\partial^2 u_0}{\partial T^2} + \bar{I}_1 \frac{\partial^2 \phi_x}{\partial T^2} \tag{19}$$

$$\frac{\partial N_{xy}}{\partial X} + \frac{\partial N_{yy}}{\partial Y} = \bar{I}_0 \frac{\partial^2 v_0}{\partial T^2} + \bar{I}_1 \frac{\partial^2 \phi_y}{\partial T^2} \tag{20}$$

$$\frac{\partial Q_x}{\partial X} + \frac{\partial Q_y}{\partial Y} + \frac{\partial}{\partial X}\left(N_{xx}\frac{\partial w_0}{\partial X} + N_{xy}\frac{\partial w_0}{\partial Y} \right) + \frac{\partial}{\partial Y}\left(N_{xy}\frac{\partial w_0}{\partial X} + N_{yy}\frac{\partial w_0}{\partial Y} \right) + F(X,Y,T) = \bar{I}_0 \frac{\partial^2 w_0}{\partial T^2} \tag{21}$$

$$\frac{\partial M_{xx}}{\partial X} + \frac{\partial M_{xy}}{\partial Y} - Q_x = \bar{I}_2 \frac{\partial^2 \phi_x}{\partial T^2} + \bar{I}_1 \frac{\partial^2 u_0}{\partial T^2} \tag{22}$$

$$\frac{\partial M_{xy}}{\partial X} + \frac{\partial M_{yy}}{\partial Y} - Q_y = \bar{I}_2 \frac{\partial^2 \phi_y}{\partial T^2} + \bar{I}_1 \frac{\partial^2 v_0}{\partial T^2} \tag{23}$$

The inertia related terms are defined by

$$\bar{I}_i = \sum_{k=1}^{N_L} \int_{Z_k}^{Z_{k+1}} Z^i \rho^{(k)} \mathrm{d}Z \quad (i = 0, 1, 2) \tag{24}$$

where $\rho^{(k)}$ is the mass density of the kth layer. The axial forces (N_{xx} , N_{yy}, N_{xy}), bending moments (M_{xx} , M_{yy}, M_{xy}) and shear forces (Q_x , Q_y) are related to strain components by

$$\begin{Bmatrix} N_{xx} \\ N_{yy} \\ N_{xy} \end{Bmatrix} = \left[\bar{A}\right] \begin{Bmatrix} \varepsilon_{xx}^{(0)} \\ \varepsilon_{yy}^{(0)} \\ \gamma_{xy}^{(0)} \end{Bmatrix} + \left[\bar{B}\right] \begin{Bmatrix} \varepsilon_{xx}^{(1)} \\ \varepsilon_{yy}^{(1)} \\ \gamma_{xy}^{(1)} \end{Bmatrix} \tag{25}$$

$$\begin{Bmatrix} M_{xx} \\ M_{yy} \\ M_{xy} \end{Bmatrix} = \left[\bar{B}\right] \begin{Bmatrix} \varepsilon_{xx}^{(0)} \\ \varepsilon_{yy}^{(0)} \\ \gamma_{xy}^{(0)} \end{Bmatrix} + \left[\bar{D}\right] \begin{Bmatrix} \varepsilon_{xx}^{(1)} \\ \varepsilon_{yy}^{(1)} \\ \gamma_{xy}^{(1)} \end{Bmatrix} \tag{26}$$

$$\begin{Bmatrix} Q_y \\ Q_x \end{Bmatrix} = k_S \left[\bar{K}\right] \begin{Bmatrix} \gamma_{yz}^{(0)} \\ \gamma_{xz}^{(0)} \end{Bmatrix} \tag{27}$$

where shear correction factor $k_S = 5/6$. The stiffness elements $\bar{A}_{ij}, \bar{B}_{ij}, \bar{D}_{ij}$, and $\bar{K}_{ij}$ of the plate are defined as

$$(\bar{A}_{ij}, \bar{B}_{ij}, \bar{D}_{ij}) = \sum_{k=1}^{N_L} \int_{Z_k}^{Z_{k+1}} P_{ij}^{(k)} (1, Z, Z^2) \mathrm{d}Z, \quad (i, j = 1, 2, 3) \tag{28}$$

$$\bar{K}_{ij} = \sum_{k=1}^{N_L} \int_{Z_k}^{Z_{k+1}} Q_{ij}^{(k)} \mathrm{d}Z, \quad (i, j = 1, 2) \tag{29}$$

Substituting Eqs (25)-(27) into Eqs (19)-(23) and introducing the following dimensionless parameters

$$\begin{aligned} &x = \frac{X}{a}, \quad y = \frac{Y}{b}, \quad u = \frac{u_0}{h}, \quad v = \frac{v_0}{h}, \quad w = \frac{w_0}{h}, \quad \alpha = \frac{h}{a}, \\ &\beta = \frac{a}{b}, \quad t = \frac{T}{h}\sqrt{\frac{E_{\mathrm{M}}}{\rho_{\mathrm{M}}}}, \quad A_{ij} = \frac{\bar{A}_{ij}}{E_{\mathrm{M}} a}, \quad B_{ij} = \frac{\bar{B}_{ij}}{E_{\mathrm{M}} a^2}, \\ &D_{ij} = \frac{\bar{D}_{ij}}{E_{\mathrm{M}} a^3}, \quad K_{ij} = \frac{\bar{K}_{ij}}{E_{\mathrm{M}} a}, \quad I_i = \frac{\bar{I}_i}{\rho_{\mathrm{M}} h^{i+1}}, \quad f = \frac{F}{E_{\mathrm{M}}} \end{aligned} \tag{30}$$

the governing equations can be rewritten in terms of dimensionless displacements $(u, v, w, \phi_x, \phi_y)$

$$L_{11}u + L_{12}v + L_{13}\phi_x + L_{14}\phi_y = I_0 \frac{\partial^2 u}{\partial t^2} + I_1 \frac{\partial^2 \phi_x}{\partial t^2} \tag{31}$$

$$L_{21}u + L_{22}v + L_{23}\phi_x + L_{24}\phi_y = I_0 \frac{\partial^2 v}{\partial t^2} + I_1 \frac{\partial^2 \phi_y}{\partial t^2} \tag{32}$$

$$L_{31}w + L_{32}\phi_x + L_{33}\phi_y + f = I_0 \frac{\partial^2 w}{\partial t^2} \tag{33}$$

$$L_{41}u + L_{42}v + L_{43}w + L_{44}\phi_x + L_{45}\phi_y = I_1 \frac{\partial^2 u}{\partial t^2} + I_2 \frac{\partial^2 \phi_x}{\partial t^2} \tag{34}$$

$$L_{51}u + L_{52}v + L_{53}w + L_{54}\phi_x + L_{55}\phi_y = I_1\frac{\partial^2 v}{\partial t^2} + I_2\frac{\partial^2 \phi_y}{\partial t^2} \tag{35}$$

where the expressions of partial differential operators L_{ij} are given in Appendix A.

It is assumed that the plate is simply supported at all edges with boundary conditions

$$v = w = \phi_y = N_{xx} = M_{xx} = 0 \quad \text{at} x = 0,1 \tag{36}$$

$$u = w = \phi_x = N_{yy} = M_{yy} = 0 \quad \text{at} y = 0,1 \tag{37}$$

3. Solution procedure

3.1 Forced vibration analysis

Galerkin's method is used to obtain the analytical solution for the governing partial differential Eqs (31)-(35) under boundary conditions specified in Eqs (36) and (37). The dimensionless displacements are expressed in double Fourier series as

$$u(x,y,t) = \sum_{m=1}^{M}\sum_{n=1}^{N} U_{mn}(t)\cos m\pi x \sin n\pi y \tag{38}$$

$$v(x,y,t) = \sum_{m=1}^{M}\sum_{n=1}^{N} V_{mn}(t)\sin m\pi x \cos n\pi y \tag{39}$$

$$w(x,y,t) = \sum_{m=1}^{M}\sum_{n=1}^{N} W_{mn}(t)\sin m\pi x \sin n\pi y \tag{40}$$

$$\phi_x(x,y,t) = \sum_{m=1}^{M}\sum_{n=1}^{N} X_{mn}(t)\cos m\pi x \sin n\pi y \tag{41}$$

$$\phi_y(x,y,t) = \sum_{m=1}^{M}\sum_{n=1}^{N} Y_{mn}(t)\sin m\pi x \cos n\pi y \tag{42}$$

where $U_{mn}(t)$, $V_{mn}(t)$, $W_{mn}(t)$, $X_{mn}(t)$, and $Y_{mn}(t)$ are unknown functions of dimensionless time t.

Substituting Eqs (38)-(42) into Eqs (31)-(35), multiplying the equations by $\cos p\pi x \sin q\pi y$, $\sin p\pi x \cos q\pi y$, $\sin p\pi x \sin q\pi y$, $\cos p\pi x \sin q\pi y$ and $\sin p\pi x \cos q\pi y$, respectively, in which p and q are positive integers; then integrating the resulting equations with respect to x from 0 to 1 and y from 0 to 1, the spatially discretized equations of the plate can be derived as follows

$$[M]\{\ddot{\Delta}\}+[S]\{\Delta\}=\{Q\} \tag{43}$$

where

$$[M]=\begin{bmatrix} m_{11} & 0 & 0 & 0 & 0 \\ 0 & m_{22} & 0 & 0 & 0 \\ 0 & 0 & m_{33} & 0 & 0 \\ 0 & 0 & 0 & m_{44} & 0 \\ 0 & 0 & 0 & 0 & m_{55} \end{bmatrix},\quad [S]=\begin{bmatrix} s_{11} & s_{12} & s_{13} & s_{14} & s_{15} \\ s_{21} & s_{22} & s_{23} & s_{24} & s_{25} \\ s_{31} & s_{32} & s_{33} & s_{34} & s_{35} \\ s_{41} & s_{42} & s_{43} & s_{44} & s_{45} \\ s_{51} & s_{52} & s_{53} & s_{54} & s_{55} \end{bmatrix},$$
$$\{\Delta\}=\begin{Bmatrix} U_{mn} \\ V_{mn} \\ W_{mn} \\ X_{mn} \\ Y_{mn} \end{Bmatrix},\quad \{Q\}=\begin{Bmatrix} 0 \\ 0 \\ Q_{mn} \\ 0 \\ 0 \end{Bmatrix},\quad Q_{mn}=4\int_0^1\int_0^1 f\sin p\pi x\sin q\pi y\mathrm{d}x\mathrm{d}y \tag{44}$$

The details of all elements in matrices [*M*] and [*S*] are given in Appendix B.

Eq. (43) is then solved by the variable-step fourth-fifth-order Runge-Kutta method [35] to determine the forced response of the plate.

3.2 Free vibration analysis

Free vibration can be treated as a subset problem in Eq. (43). For harmonic vibration, let

$$\{\Delta\}=\{\Delta\}_0 e^{i\omega t} \tag{45}$$

where ω is the dimensionless natural frequency, $\{\Delta\}_0=\left\{U_{mn}^0 \quad V_{mn}^0 \quad W_{mn}^0 \quad X_{mn}^0 \quad Y_{mn}^0\right\}^T$ is the unknown coefficients associated with displacement components. Substituting Eq. (45) into Eq. (43) and dropping off the force vector $\{Q\}$, the following eigenvalue equation is obtained

$$\left([S]-\omega^2[M]\right)\{\Delta\}_0=\{0\} \tag{46}$$

The natural frequencies can be found from the nontrivial solution of Eq. (46).

4. Results and discussion

A detailed parametric study is conducted in this section to investigate the free and forced vibrations of the multi-layer functionally graded GPL/polymer plates, with a particular focus on the effects of the distribution pattern, weight fraction, length-to-thickness and length-to-width ratios of GPLs, and the

total number of layers on the dynamic characteristics of the plate. Numerical results are presented in both tabular and graphical forms.

4.1 Free vibration

As there are no results available for the vibration behavior of graphene based nanocomposite plates in open literature, a simply supported aluminum/alumina (Al/Al_2O_3) functionally graded square plate is used as an example and its dimensionless natural frequency $\bar{\omega} = \omega h\sqrt{\rho_2 / E_2}$ is compared with the existing ones [36] in Table 1 to validate the present analysis. The material properties are

$$\begin{aligned} &\text{Al:} \quad E_1 = 70.0\times10^9\,\text{N/m}^2, \quad \nu_1 = 0.3, \quad \rho_1 = 2702\text{kg/m}^3 \\ &Al_2O_3\text{:} \quad E_2 = 380\times10^9\,\text{N/m}^2, \quad \nu_2 = 0.3, \quad \rho_2 = 3800\text{kg/m}^3 \end{aligned} \tag{47}$$

It is assumed that the top and bottom surfaces of the plate are Al and Al_2O_3 rich, respectively. The effective material properties through the thickness, $P(z)$, follow a power law distribution [37]

$$P(Z) = P_1 + (P_2 - P_1)\left(\frac{1}{2} + \frac{Z}{h}\right)^{\vartheta} \quad (\vartheta \geq 0) \tag{48}$$

where P_1 and P_2 denote the properties of Al and Al_2O_3, respectively, and ϑ is the volume fraction index. By employing the equivalent homogenous laminated structure approach [38-40], a functionally graded plate is divided into a finite number of isotropic and homogenous layers along the thickness direction and the equivalent effective material property of each layer is defined as the average value of Eq. (48) within the layer as [40]

$$P_{eq}^{(k)} = \int_{Z_k}^{Z_{k+1}} \frac{P(Z)}{Z_{k+1} - Z_k} \mathrm{d}Z, \quad k = 1,2,...,N_L \tag{49}$$

As can be observed, our results converge monotonically as the number of layers increases and are in excellent agreement with the higher-order deformation plate theory based results [36]. The maximum difference is 1.30% for the plate with a/h = 5, and 0.38% for the plate with a/h = 10.

Table 1. Dimensionless fundamental natural frequency $\bar{\omega} = \omega h\sqrt{\rho_2 / E_2}$ of a simply supported Al/Al_2O_3 functionally graded square plate

a/h	N_L	ϑ				
		0.0	0.5	1.0	4.0	10.0
5						

	10	0.2112	0.1809	0.1634	0.1393	0.1316
	20	0.2112	0.1806	0.1632	0.1396	0.1322
	30	0.2112	0.1805	0.1631	0.1396	0.1323
	40	0.2112	0.1805	0.1631	0.1396	0.1323
	Ref. [36]	0.2121	0.1819	0.1640	0.1383	0.1306
10						
	10	0.05769	0.04912	0.04427	0.03811	0.03632
	20	0.05769	0.04903	0.04421	0.03820	0.03651
	30	0.05769	0.04901	0.04420	0.03822	0.03655
	40	0.05769	0.04901	0.04420	0.03823	0.03656
	Ref. [36]	0.05777	0.04917	0.04426	0.03811	0.03642

In what follows, epoxy is chosen as the polymer matrix. Unless otherwise stated, the plate ($a\times b\times h = 0.45\text{m}\times 0.45\text{m}\times 0.045\text{m}$) is reinforced with GPLs with dimensions $l_{\text{GPL}} = 2.5\mu\text{m}$, $w_{\text{GPL}} = 1.5\mu\text{m}$, $h_{\text{GPL}} = 1.5\text{nm}$. The material properties of GPLs and epoxy are $\rho_{\text{GPL}} = 1.06\text{g/cm}^3$, $E_{\text{GPL}} = 1.01\text{TPa}$, $\rho_{\text{M}} = 1.2\text{g/cm}^3$ [6]; $E_{\text{M}} = 3.0\text{GPa}$, $\nu_{\text{M}} = 0.34$ [41]; $\nu_{\text{GPL}} = 0.186$ [42]. In addition, GPL weight fraction is 1%, and the total number of layers $N_L = 10$.

Dimensionless natural frequencies of multi-layer functionally graded GPL/polymer plates with different GPL distribution patterns are listed in Table 2 where the value in the bracket denotes the percentage frequency increase due to the addition of GPL reinforcing nanofillers. Fig. 3 investigates the effect of GPL weight fraction on the fundamental frequency change of the nanocomposite plates with different GPL distribution patterns.

Table 2. Dimensionless natural frequencies of plates: Effect of GPL distribution patterns

m, *n*	Pure epoxy	Pattern 1	Pattern2	Pattern 3	Pattern 4
1, 1	0.0584	0.1216(108.2%)	0.1020(74.7%)	0.1378(136.0%)	0.1118(91.4%)
2, 1	0.1391	0.2895(108.1%)	0.2456(76.6%)	0.3249(133.6%)	0.2673(92.2%)
2, 2	0.2132	0.4436(108.1%)	0.3796(78.0%)	0.4939(131.7%)	0.4110(92.8%)
3, 1	0.2595	0.5400(108.1%)	0.4645(79.0%)	0.5984(130.6%)	0.5013(93.2%)
3, 2	0.3251	0.6767(108.2%)	0.5860(80.3%)	0.7454(129.3%)	0.6299(93.8%)
3, 3	0.4261	0.8869(108.1%)	0.7755(82.0%)	0.9690(127.4%)	0.8287(94.5%)

Note: The percentage value in parentheses denotes the relative frequency increase $(\omega_{\text{C}} - \omega_{\text{M}})/\omega_{\text{M}}$, in which ω_{C} and ω_{M} are natural frequencies with and without GPLs, respectively.

Numerical results show that the improvement in plate stiffness hence the fundamental natural frequency through the incorporation of GPLs is very impressive. For example, the fundamental natural

frequency of the plate with the addition of 1.2% weight fraction of GPLs is approximately 160% higher than that of the pristine epoxy plate. The frequencies also increase with GPL concentration increases no matter how they are distributed in the epoxy matrix. As can be observed from both Table 2 and Fig. 3, the GPL distribution pattern plays an important role in improving the dynamic characteristics of the plate. At the same amount of GPLs additives, distribution pattern 3 gives the highest fundamental frequency which is over 60% bigger than the lowest fundamental frequency produced by distribution pattern 2. This clearly indicates that dispersing more GPL nanofillers near the top and bottom surfaces of the plate where very high normal stress is located and much less content near its mid-plane where the normal stress is very small is the most effective way to strengthen plate stiffness for remarkably increased natural frequencies. This is due to the fact that such a distribution can make the best use of the high modulus GPL nanofillers therefore leads to the biggest increase in plate stiffness elements $\bar{A}_{ij}$, $\bar{B}_{ij}$, $\bar{D}_{ij}$ and $\bar{K}_{ij}$.

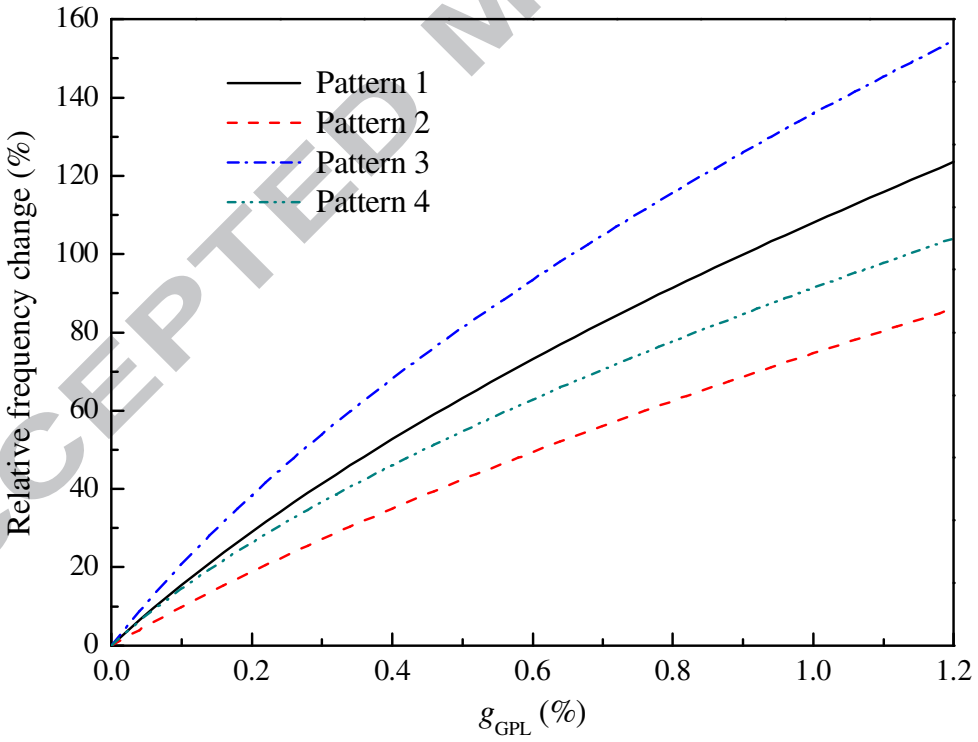

Fig. 3. Effect of GPL weight fraction on the percentage fundamental frequency change for GPL/epoxy plates with different distribution patterns

Fig. 4 presents the effects of the geometry and size of GPL nanofillers, in terms of length-to-

thickness ratio l_{GPL}/h_{GPL} and length-to-width ratio l_{GPL}/w_{GPL}, on dimensionless fundamental frequency of the GPL/epoxy nanocomposite plate, where the GPL length l_{GPL} remains a constant. Note that l_{GPL}/w_{GPL}= 1 and l_{GPL}/w_{GPL}≠ 1 correspond to a square shaped GPL and a rectangular shaped GPL, respectively. A significant increase in natural frequency is observed as the l_{GPL}/h_{GPL} ratio increases all the way up to l_{GPL}/h_{GPL} = 1000, followed by a slight further increase as l_{GPL}/h_{GPL} further increases. Since a higher l_{GPL}/h_{GPL} ratio virtually represents GPLs with less graphene layers, this observation clearly indicates that GPLs with fewer layers would be more effective in improving the natural frequencies. Results also show that, regardless of how GPLs are distributed, the plate reinforced with square GPLs (l_{GPL}/w_{GPL}= 1) has larger natural frequencies than that reinforced with rectangular GPLs (l_{GPL}/w_{GPL}= 2). In other words, GPLs with a larger surface area are better reinforcing nanofillers than their counterparts with a smaller surface area. This is because with the same amount of GPLs, a larger contact area between the polymer matrix and the GPLs provides better load transfer thus leading to higher structural stiffness.

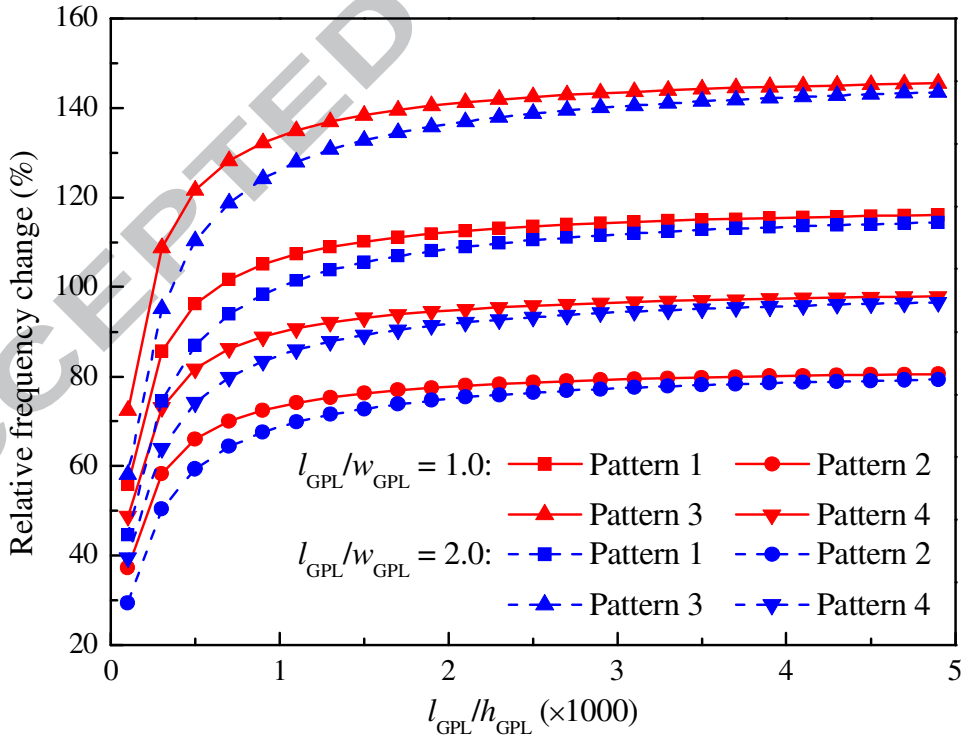

Fig. 4. Effects of GPL length-to-thickness and length-to-width ratios on the percentage fundamental

frequency change for GPL/epoxy nanocomposite plates.

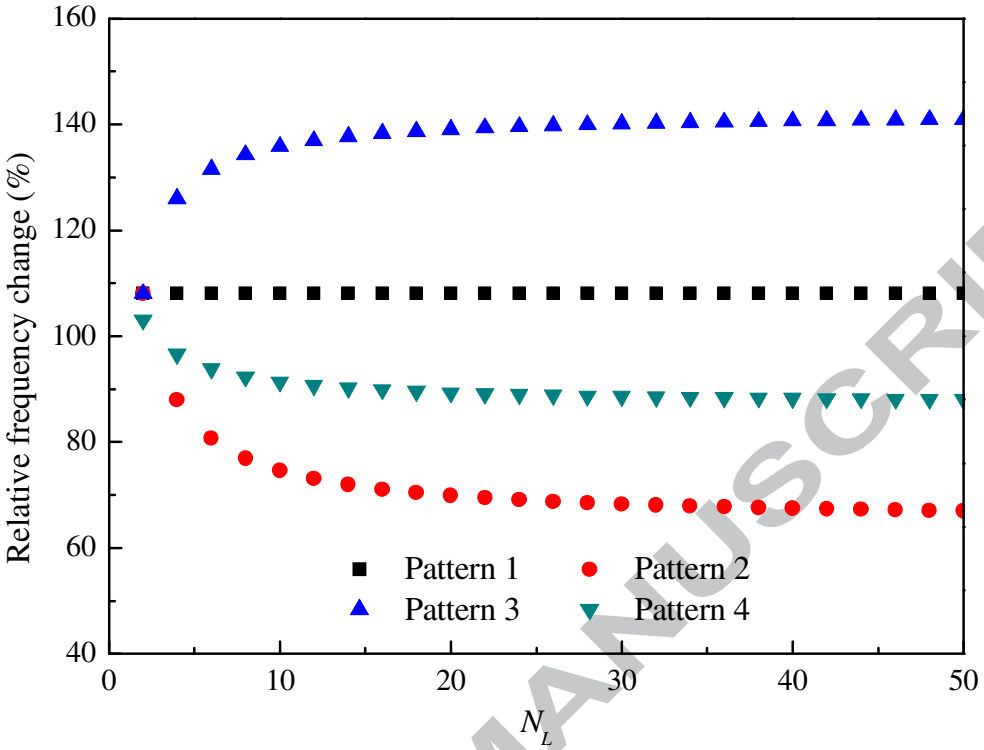

Fig. 5. Effect of total number of layers N_L on the percentage fundamental frequency change for GPL/epoxy nanocomposite plates

Fig. 5 shows the relative frequency change of the GPL/epoxy plates with different total number of layers N_L. As expected, the fundamental frequencies of the plates with GPL distribution pattern 1 are not affected by N_L since they are homogeneous. For plates where GPLs are non-uniformly dispersed, their fundamental frequencies decrease as the total number of layer increases to N_L = 10 ~15 then remain almost unchanged when N_L is further increased for GPL distribution patterns 2 and 4. This trend, however, is reversed for GPL distribution pattern 3. Among the three non-uniform patterns considered, the fundamental frequency of the plate with GPL pattern 4 is least affected by the change in N_L.

4.2 Forced vibration

For the forced vibration analysis in this section, a triangular pressure pulse load shown in Fig. 6 is considered as an example which is expressed as

$$F(X,Y,T)=\begin{cases} P_m(1-T/T_p), & 0\le T\le T_p \\ 0, & T<0 \text{ and } T>T_p \end{cases} \tag{50}$$

where P_m is the peak pulse pressure, T_p is the duration of the pulse loading. Then in Eq. (44),

$Q_{mn}=\begin{cases}\dfrac{4\lambda_{mn}p_m}{mn\pi^2}\left(1-t/t_p\right), & 0\le t\le t_p\\ 0, & t<0 \text{ and } t>t_p\end{cases}$, in which $\lambda_{mn}=1-(-1)^m-(-1)^n+(-1)^{m+n}$, $p_m=\dfrac{P_m}{E_{\mathrm{M}}}$, and $t_p=\dfrac{T_p}{h}\sqrt{\dfrac{E_{\mathrm{M}}}{\rho_{\mathrm{M}}}}$. In what follows, it is assumed that the peak pulse pressure is $P_m=500k\mathrm{Pa}$ and the duration of the loading T_p is 0.01s.

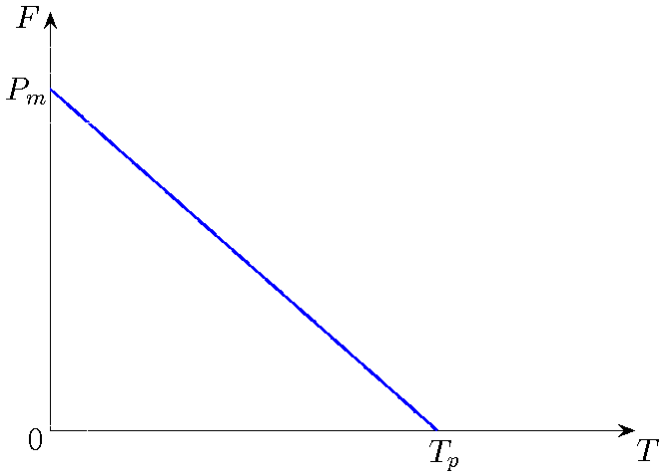

Fig. 6. A triangular pressure pulse load

Convergence study is first conducted in Fig. 7 where the dimensionless central deflection responses of a GPL/epoxy nanocomposite plate (GPL distribution pattern 2, N_L = 10) when $M = N = 1$ and $M = N = 5$ are compared. As can be observed, one term solution ($M = N = 1$) in double Fourier series (39)-(43) are sufficient to yield a convergent result. Since there are no existing results available in the open literature for the dynamic analysis of functionally graded GPL/polymer nanocomposite plates, our results are compared in Fig. 8 with the finite element (FE) results obtained by using commercial software package ABAQUS for the dimensionless central deflection response of a pristine epoxy plate and a nanocomposite plate with GPL distribution pattern 2. In the FE model, four-node conventional shell elements (S4R) with 40×40 mesh grid are used. Excellent agreement is achieved.

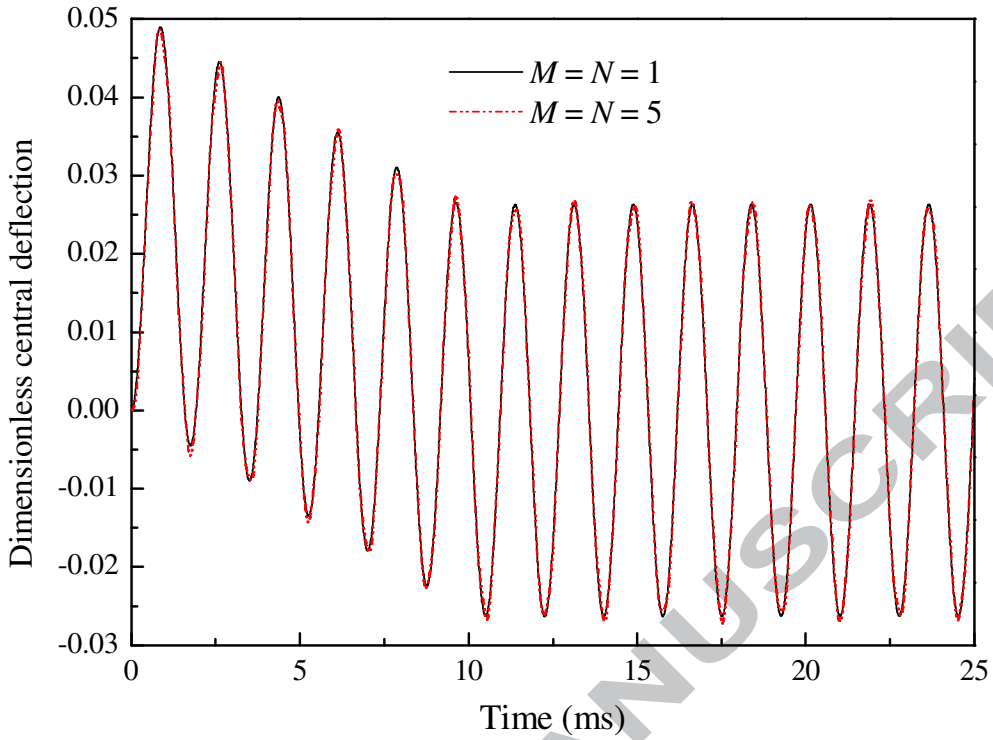

Fig. 7. Dimensionless central deflection response of a GPL/epoxy nanocomposite plate: Convergence study.

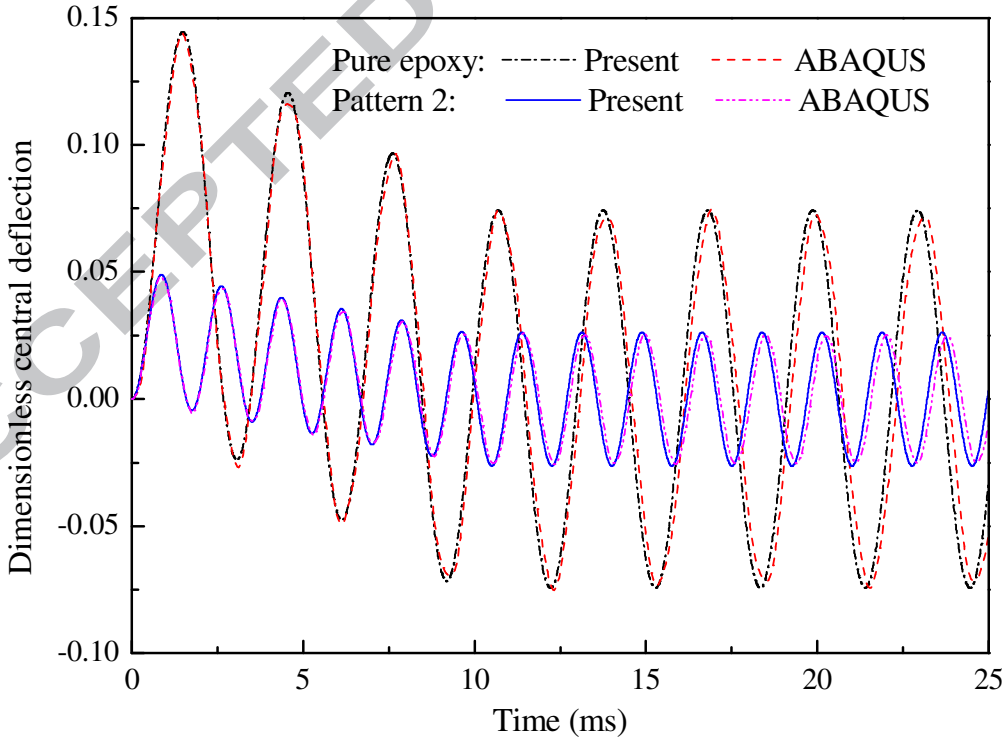

Fig. 8. Dimensionless central deflection responses of a pristine epoxy plate and a GPL/epoxy

nanocomposite plate: Comparison with FE results

Fig. 9 compares the dimensionless central deflection responses of a pure epoxy plate and GPL/epoxy nanocomposite plates with different GPL distribution patterns. Apparently, the pristine epoxy plate has much larger dynamic response than those reinforced by GPLs. This demonstrates the significant reinforcing effect of adding a very small amount of GPLs into the polymer matrix.

Fig. 10 displays the effect of GPL weight fraction g_{GPL} on the maximum deflection ratio $f_{\mathrm{C}} / f_{\mathrm{M}}$ for different distribution patterns in which f_{C} and f_{M} denote the maximum dynamic central deflection of the plates with and without GPLs, respectively. It is obvious that a smaller $f_{\mathrm{C}} / f_{\mathrm{M}}$ ratio corresponds to a stronger reinforcing effect by the incorporation of GPLs. A remarkable drop in dynamic deflection is seen as the weight fraction g_{GPL} increases. For example, distributing only 1.0% weight fraction GPLs according to distribution pattern 3 can yield a significantly lower dynamic central deflection that is only 20% of that of the pure epoxy plate.

Similar to the observations in free vibration analysis, results in Figs. 9 and 10 show that the way GPLs are distributed also plays an important role in the dynamic response of the plate. The symmetric distribution pattern 3 gives the lowest dynamic deflection, followed by uniform pattern 1, asymmetric pattern 4 then symmetric pattern 2 which is considered to be the most unfavorable way for dispersing GPLs. This again verifies that at the same amount of GPLs, dispersion of more GPL nanofillers near the top and bottom surfaces of plates is the most effective way to reduce the dynamic responses of plates.

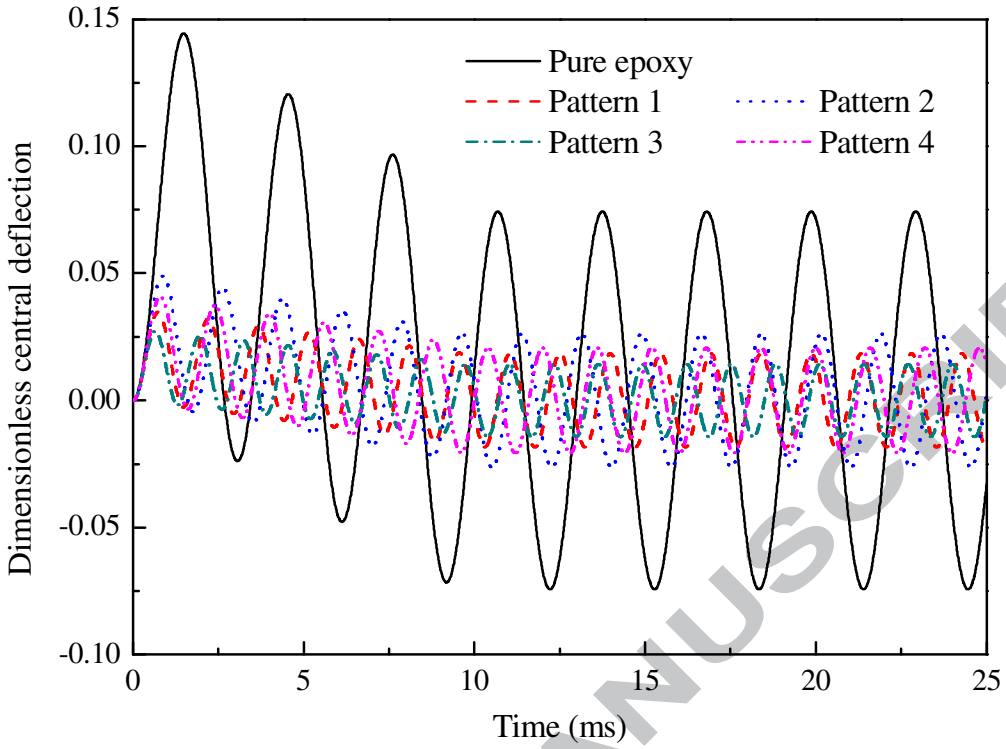

Fig. 9. Dimensionless central deflection responses of GPL/epoxy nanocomposite plates.

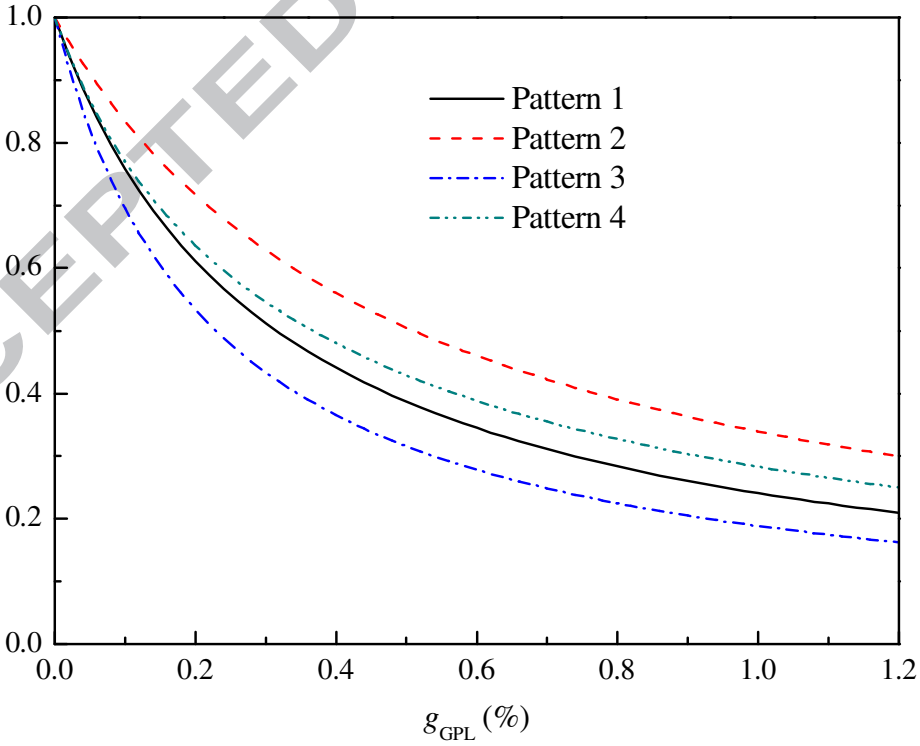

Fig. 10. Effect of GPL weight fraction on f_C / f_M for GPL/epoxy nanocomposite plates.

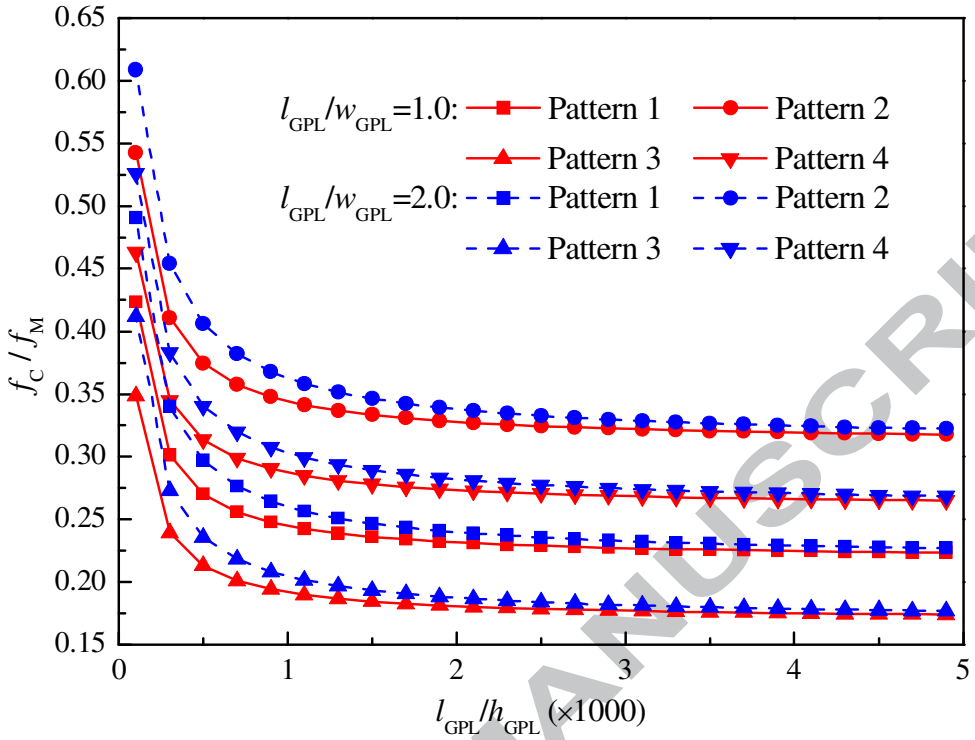

Fig. 11. Effects of GPL length-to-thickness and length-to-width ratios on f_C / f_M for GPL/epoxy nanocomposite plates.

Fig. 11 studies the effects of GPL length-to-thickness ratio l_{GPL} / h_{GPL} and length-to-width ratio l_{GPL} / w_{GPL} on the maximum dynamic deflection ratio f_C / f_M for GPL/epoxy nanocomposite plates with different distributed patterns. Results show that compared with rectangular shaped GPLs (l_{GPL} / w_{GPL} = 2.0), square shaped GPLs (l_{GPL} / w_{GPL} = 1.0) are better reinforcing nanofillers that lead to lower dynamic deflection. The maximum dynamic deflection is significantly reduced as l_{GPL} / h_{GPL} ratio increases, or, in other words, by using GPLs with fewer graphene single layers. However, a further increase in l_{GPL} / h_{GPL} when it goes beyond 1000 will bring a fairly slightly decreased dynamic deflection only.

The effect of the total number of layers N_L on the maximum dynamic deflection ratio f_C / f_M of GPL/epoxy nanocomposite plates is illustrated in Fig. 12. As can be observed, the dynamic deflection

increases with an increase in N_L for both GPL distribution patterns 2 and 4 but becomes lower for distribution pattern 3. When $N_L \geq$ 10~15, however, the dynamic deflection tends to be almost constant even when N_L is further increased. For each distribution pattern, 10 layers are enough to obtain its corresponding converged result for the dynamic response. This is consistent with the free vibration results in Figure 5, both indicating that from manufacturing perspective, the multi-layer structure with 10~15 layers stacked up would be accurate enough to approximate the desired continuous and smooth through-thickness change in GPL distribution which is impossible to be fabricated due to the constraint of current manufacturing technology in graphene-based nanocomposites.

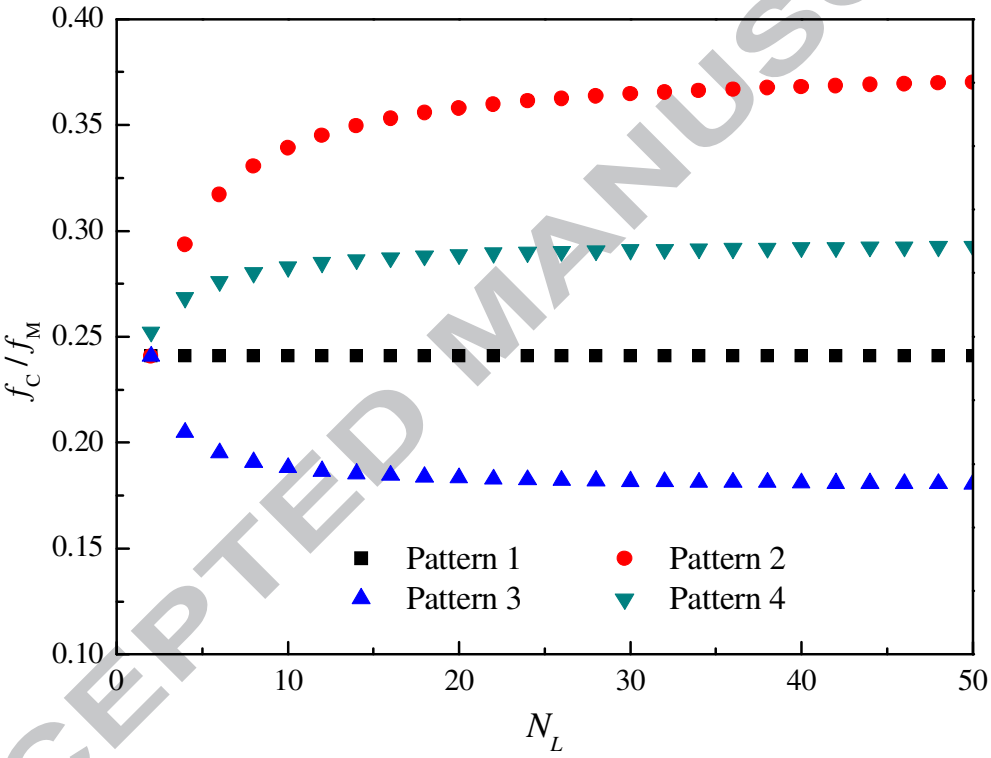

Fig. 12. Effect of total number of layers N_L on f_C / f_M for GPL/epoxy nanocomposite plates.

5. **Conclusions**

Free and forced vibration behaviors of functionally graded multilayer GPL/polymer nanocomposite plates have been investigated within the framework of the first-order shear deformation theory. Navier solution based technique is employed to obtain the natural frequencies and dynamic response of simply supported plates subjected to a pulse loading. The effects of GPL distribution pattern, weight fraction, geometry and size as well as the total number of layers on the dynamic characteristics of the plates are

investigated in detail through a parametric study. It is found that (1) an addition of a very small amount of GPLs can significantly increase the natural frequencies and reduce the forced vibration response of the plates; (2) dispersing more square shaped GPLs consisting of fewer single graphene layers near the top and bottom surfaces of the plate is the most effective way to reinforce the plate for increased natural frequencies and remarkably reduced dynamic deflections; (3) A multilayer structure with 10~15 individual layers stacked up can achieve the desired functionally graded compositional profile with sufficient accuracy yet relatively low manufacturing cost.

Acknowledgements

This work is fully funded by a research grant from the Australian Research Council under Discovery Project scheme (DP160101978). The authors are grateful for the financial support. Dr. Mitao Song is also grateful for the support from the National Natural Science Foundation of China (Grant No. 11302087).

References

[1] Bellucci S, Balasubramanian C, Micciulla F, Rinaldi G. CNT composites for aerospace applications. Journal of Experimental Nanoscience 2007; 2(3): 193-206.

[2] Adam H. Carbon fibre in automotive applications. Materials & Design 1997; 18(4-6): 349-355.

[3] Gauvin F, Robert M. Durability study of vinylester/silicate nanocomposites for civil engineering applications. Polymer Degradation and Stability 2015; 121: 359-368.

[4] Baradaran S, Moghaddam E, Basirun WJ, Mehrali M, Sookhakian M, Hamdi M, Nakhaei Moghaddam MR, Alias Y. Mechanical properties and biomedical applications of a nanotube hydroxyapatite-reduced graphene oxide composite. Carbon 2014; 69: 32-45.

[5] Huang X, Qi X, Boey F, Zhang H. Graphene-based composites. Chemical Society Reviews 2012; 41(2): 666-686.

[6] Rafiee MA, Rafiee J, Wang Z, Song H, Yu Z-Z, Koratkar N. Enhanced mechanical properties of nanocomposites at low graphene content. ACS Nano 2009; 3(12): 3884-3890.

[7] Rafiee MA, Rafiee J, Yu Z-Z, Koratkar N. Buckling resistant graphene nanocomposites. Applied Physics Letters 2009; 95(22): 223103.

[8] Rafiee MA, Rafiee J, Srivastava I, Wang Z, Song H, Yu Z-Z, Koratkar N. Fracture and fatigue in graphene nanocomposites. Small 2010; 6(2): 179-183.

[9] Potts JR, Dreyer DR, Bielawski CW, Ruoff RS. Graphene-based polymer nanocomposites. Polymer 2011; 52(1): 5-25.

[10] Montazeri A, Rafii-Tabar H. Multiscale modeling of graphene- and nanotube-based reinforced polymer nanocomposites. Physics Letters A 2011; 375(45): 4034-4040.

[11] Mortazavi B, Benzerara O, Meyer H, Bardon J, Ahzi S. Combined molecular dynamics-finite element multiscale modeling of thermal conduction in graphene epoxy nanocomposites. Carbon 2013; 60: 356-365.

[12] Wang Y, Yu J, Dai W, Song Y, Wang D, Zeng L, Jiang N. Enhanced thermal and electrical properties of epoxy composites reinforced with graphene nanoplatelets. Polymer Composites 2015; 36(3): 556-565.

[13] King JA, Klimek DR, Miskioglu I, Odegard GM. Mechanical properties of graphene nanoplatelet/epoxy composites. Journal of Applied Polymer Science 2013; 128(6): 4217-4223.

[14] Fang M, Wang K, Lu H, Yang Y, Nutt S. Covalent polymer functionalization of graphene nanosheets and mechanical properties of composites. Journal of Materials Chemistry 2009; 19(38): 7098-7105.

[15] Zhao X, Zhang Q, Chen D, Lu P. Enhanced mechanical properties of graphene-based poly(vinyl alcohol) composites. Macromolecules 2010; 43(5): 2357-2363.

[16] Wang F, Drzal LT, Qin Y, Huang Z. Mechanical properties and thermal conductivity of graphene nanoplatelet/epoxy composites. Journal of Materials Science 2015; 50(3): 1082-1093.

[17] Ji X-Y, Cao Y-P, Feng X-Q. Micromechanics prediction of the effective elastic moduli of graphene sheet-reinforced polymer nanocomposites. Modelling and Simulation in Materials Science and Engineering 2010; 18(4): 045005.

[18] Rahman R, Haque A. Molecular modeling of crosslinked graphene-epoxy nanocomposites for

characterization of elastic constants and interfacial properties. Composites: Part B 2013; 54: 353-364.

[19] Liu F, Hu N, Ning H, Liu Y, Li Y, Wu L. Molecular dynamics simulation on interfacial mechanical properties of polymer nanocomposites with wrinkled graphene. Computational Materials Science 2015; 108: 160-167.

[20] Spanos KN, Georgantzinos SK, Anifantis NK. Mechanical properties of graphene nanocomposites: A multiscale finite element prediction. Composite Structures 2015; 132: 536-544.

[21] Shen H-S. Nonlinear bending of functionally graded carbon nanotube-reinforced composite plates in thermal environments. Composite Structures 2009; 91(1): 9-19.

[22] Wu HL, Yang J, Kitipornchai S. Nonlinear vibration of functionally graded carbon nanotube-reinforced composite beams with geometric imperfections. Composites Part B: Engineering 2016; 90: 86-96.

[23] Rafiee M, Yang J, Kitipornchai S. Thermal bifurcation buckling of piezoelectric carbon nanotube reinforced composite beams. Computers and Mathematics with Applications 2013; 66(7): 1147-1160.

[24] Rafiee M, Yang J, Kitipornchai S. Large amplitude vibrations of carbon nanotube reinforced composite beams with piezoelectric layers. Composite Structures 2013; 96: 716-725.

[25] Ke LL, Yang J, Kitipornchai S. Nonlinear free vibration of functionally graded carbon nanotube-reinforced composite beams. Composite Structures 2010; 92(3): 676-683.

[26] Ke LL, Yang J, Kitipornchai S. Dynamic stability of functionally graded carbon nanotube-reinforced composite beams. Mechanics of Advanced Materials and Structures. 2013; 20 (1): 28-37.

[27] Wu HL, Kitipornchai S, Yang J. Free vibration and buckling analysis of sandwich beams with functionally graded carbon nanotube-reinforced composite face sheets. International Journal of Structural Stability and Dynamics 2015; 15 (7): 1540011 (17 pages).

[28] Ansari R, Shojaei MF, Mohammadi V, Gholami R, Sadeghi F. Nonlinear forced vibration analysis of functionally graded carbon nanotube-reinforced composite Timoshenko beams. Composite Structures 2014; 113: 316-327.

[29] Long XJ, Li B, Wang L, Huang JY, Zhu J, Luo SN. Shock response of Cu/graphene nanolayered composites. Carbon 2016; 103: 457-463.

[30] Rissanou AN, Power AJ, Harmandaris V. Structural and dynamical properties of polyethylene/graphene nanocomposites through molecular dynamics simulations. Polymers 2015; 7(3): 390-417.

[31] Chandra Y, Chowdhury R, Scarpa F, Adhikari S, Sienz J, Arnold C, Murmu T, Bould D. Vibration frequency of graphene based composites: A multiscale approach. Materials Science and Engineering B 2012; 177(3): 303-310.

[32] Guzmán de Villoria R, Miravete A. Mechanical model to evaluate the effect of the dispersion in nanocomposites. Acta Materialia 2007; 55(9): 3025-3031.

[33] Halpin JC, Kardos JL. The Halpin-Tsai equations: a review. Polymer Engineering & Science 1976; 16(5): 344-352.

[34] Reddy JN. Mechanics of laminated composite plates and shells: theory and analysis. CRC Press; 2004.

[35] Cash JR, Karp AH. A variable order Runge-Kutta method for initial value problems with rapidly varying right-hand sides. ACM Transactions on Mathematical Software 1990; 16(3): 201-222.

[36] Matsunaga H. Free vibration and stability of functionally graded plates according to a 2-D higher-order deformation theory. Composite Structures 2008; 82(4): 499-512.

[37] Reddy JN, Cheng Z-Q. Three-dimensional solutions of smart functionally graded plates. Journal of Applied Mechanics-Transactions of the ASME 2001; 68(2): 234-241.

[38] Ramirez F, Heyliger PR, Pan E. Static analysis of functionally graded elastic anisotropic plates using a discrete layer approach. Composites: Part B 2006; 37(1): 10-20.

[39] Shakeri M, Mirzaeifar R. Static and dynamic analysis of thick functionally graded plates with piezoelectric layers using layerwise finite element model. Mechanics of Advanced Materials and Structures 2009; 16(8): 561-575.

[40] Aksoylar C, Omercikoglu A, Mecitoglu Z, Omurtag MH. Nonlinear transient analysis of FGM and FML plates under blast loads by experimental and mixed FE methods. Composite Structures 2012; 94(2): 731-744.

[41] Yasmin A, Daniel IM. Mechanical and thermal properties of graphite platelet/epoxy composites.

Polymer 2004; 45(24): 8211-8219.

[42] Liu F, Ming P, Li J. Ab initio calculation of ideal strength and phonon instability of graphene under tension. Physical Review B 2007; 76(6): 064120.

Appendix A

The differential operators in Eqs. (31)-(35) are

$$L_{11}=\alpha A_{11}\frac{\partial^2}{\partial x^2}+\alpha\beta^2 A_{33}\frac{\partial^2}{\partial y^2},\quad L_{12}=\alpha\beta\left(A_{12}+A_{33}\right)\frac{\partial^2}{\partial x\partial y},\quad L_{13}=B_{11}\frac{\partial^2}{\partial x^2}+\beta^2 B_{33}\frac{\partial^2}{\partial y^2},$$

$$L_{14}=\beta\left(B_{12}+B_{33}\right)\frac{\partial^2\phi_y}{\partial x\partial y},$$

$$L_{21}=\alpha\beta\left(A_{12}+A_{33}\right)\frac{\partial^2}{\partial x\partial y},\quad L_{22}=\alpha A_{33}\frac{\partial^2}{\partial x^2}+\alpha\beta^2 A_{22}\frac{\partial^2}{\partial y^2},\quad L_{23}=\beta\left(B_{12}+B_{33}\right)\frac{\partial^2}{\partial x\partial y},$$

$$L_{24}=B_{33}\frac{\partial^2}{\partial x^2}+\beta^2 B_{22}\frac{\partial^2}{\partial y^2},$$

$$L_{31}=\alpha k_S K_{22}\frac{\partial^2}{\partial x^2}+\alpha\beta^2 k_S K_{11}\frac{\partial^2}{\partial y^2},\quad L_{32}=k_S K_{22}\frac{\partial}{\partial x},\quad L_{33}=\beta k_S K_{11}\frac{\partial}{\partial y},$$

$$L_{41}=B_{11}\frac{\partial^2}{\partial x^2}+\beta^2 B_{33}\frac{\partial^2}{\partial y^2},\quad L_{42}=\beta\left(B_{12}+B_{33}\right)\frac{\partial^2}{\partial x\partial y},\quad L_{43}=-k_S K_{22}\frac{\partial}{\partial x},$$

$$L_{44}=\frac{1}{\alpha}D_{11}\frac{\partial^2}{\partial x^2}+\frac{\beta^2}{\alpha}D_{33}\frac{\partial^2}{\partial y^2}-\frac{1}{\alpha}k_S K_{22},\quad L_{45}=\frac{\beta}{\alpha}\left(D_{12}+D_{33}\right)\frac{\partial^2}{\partial x\partial y},$$

$$L_{51}=\beta\left(B_{12}+B_{33}\right)\frac{\partial^2}{\partial x\partial y},\quad L_{52}=B_{33}\frac{\partial^2}{\partial x^2}+\beta^2 B_{22}\frac{\partial^2}{\partial y^2},\quad L_{53}=-\beta k_S K_{11}\frac{\partial}{\partial y},$$

$$L_{54}=\frac{\beta}{\alpha}\left(D_{12}+D_{33}\right)\frac{\partial^2}{\partial x\partial y},\quad L_{55}=\frac{1}{\alpha}D_{33}\frac{\partial^2}{\partial x^2}+\frac{\beta^2}{\alpha}D_{22}\frac{\partial^2}{\partial y^2}-\frac{1}{\alpha}k_S K_{11}.$$

Appendix B

Coefficients shown in Eq. (43) are

$$m_{11} = I_0 I_2 - I_1^2,\ \ m_{22} = I_0 I_2 - I_1^2,\ \ m_{33} = I_0,\ \ m_{44} = I_0 I_2 - I_1^2,\ \ m_{55} = I_0 I_2 - I_1^2$$

$$s_{11} = \pi^2 \left[m^2 \left(I_2 \alpha A_{11} - I_1 B_{11} \right) + \beta^2 n^2 \left(I_2 \alpha A_{33} - I_1 B_{33} \right) \right],$$

$$s_{12} = \pi^2 \beta mn \left[\left(I_2 \alpha A_{12} - I_1 B_{12} \right) + \left(I_2 \alpha A_{33} - I_1 B_{33} \right) \right],$$

$$s_{13} = -I_1 \pi k_S m K_{22},$$

$$s_{14} = \pi^2 m^2 \left(I_2 B_{11} - \frac{I_1}{\alpha} D_{11} \right) + \pi^2 \beta^2 n^2 \left(I_2 B_{33} - \frac{I_1}{\alpha} D_{33} \right) - \frac{I_1}{\alpha} k_S K_{22},$$

$$s_{15} = \pi^2 \beta mn \left[\left(I_2 B_{12} - \frac{I_1}{\alpha} D_{12} \right) + \left(I_2 B_{33} - \frac{I_1}{\alpha} D_{33} \right) \right],$$

$$s_{21} = \pi^2 \beta mn \left[\left(I_2 \alpha A_{12} - I_1 B_{12} \right) + \left(I_2 \alpha A_{33} - I_1 B_{33} \right) \right],$$

$$s_{22} = \pi^2 \left[\beta^2 n^2 \left(I_2 \alpha A_{22} - I_1 B_{22} \right) + m^2 \left(I_2 \alpha A_{33} - I_1 B_{33} \right) \right],$$

$$s_{23} = -I_1 \pi k_S \beta n K_{11},$$

$$s_{24} = \pi^2 \beta mn \left[\left(I_2 B_{12} - \frac{I_1}{\alpha} D_{12} \right) + \left(I_2 B_{33} - \frac{I_1}{\alpha} D_{33} \right) \right],$$

$$s_{25} = \pi^2 \beta^2 n^2 \left(I_2 B_{22} - \frac{I_1}{\alpha} D_{22} \right) + \pi^2 m^2 \left(I_2 B_{33} - \frac{I_1}{\alpha} D_{33} \right) - \frac{I_1}{\alpha} k_S K_{11},$$

$$s_{31} = 0,$$

$$s_{32} = 0,$$

$$s_{33} = \pi^2 \alpha k_S \left(\beta^2 n^2 K_{11} + m^2 K_{22} \right),$$

$$s_{34} = \pi k_S m K_{22},$$

$$s_{35} = \pi k_S \beta n K_{11},$$

$$s_{41} = \pi^2 \left[m^2 \left(I_0 B_{11} - I_1 \alpha A_{11} \right) + \beta^2 n^2 \left(I_0 B_{33} - I_1 \alpha A_{33} \right) \right],$$

$$s_{42} = \pi^2 \beta mn \left[\left(I_0 B_{12} - I_1 \alpha A_{12} \right) + \left(I_0 B_{33} - I_1 \alpha A_{33} \right) \right],$$

$$s_{43} = I_0 \pi k_S m K_{22},$$

$$s_{44} = \pi^2 m^2 \left(\frac{I_0}{\alpha} D_{11} - I_1 B_{11} \right) + \pi^2 \beta^2 n^2 \left(\frac{I_0}{\alpha} D_{33} - I_1 B_{33} \right) + \frac{I_0}{\alpha} k_S K_{22},$$

$$s_{45} = \pi^2 \beta mn \left[\left(\frac{I_0}{\alpha} D_{12} - I_1 B_{12} \right) + \left(\frac{I_0}{\alpha} D_{33} - I_1 B_{33} \right) \right],$$

$$s_{51} = \pi^2 \beta mn \left[\left(I_0 B_{12} - I_1 \alpha A_{12} \right) + \left(I_0 B_{33} - I_1 \alpha A_{33} \right) \right],$$

$$s_{52} = \pi^2 \left[\beta^2 n^2 \left(I_0 B_{22} - I_1 \alpha A_{22} \right) + m^2 \left(I_0 B_{33} - I_1 \alpha A_{33} \right) \right],$$

$$s_{53} = I_0 k_S \beta \pi n K_{11},$$

$$s_{54} = \pi^2 \beta mn \left[\left(\frac{I_0}{\alpha} D_{12} - I_1 B_{12} \right) + \left(\frac{I_0}{\alpha} D_{33} - I_1 B_{33} \right) \right],$$

$$s_{55} = \pi^2 \beta^2 n^2 \left(\frac{I_0}{\alpha} D_{22} - I_1 B_{22} \right) + \pi^2 m^2 \left(\frac{I_0}{\alpha} D_{33} - I_1 B_{33} \right) + \frac{I_0}{\alpha} k_S K_{11}$$